Escherichia coli self-organizes developmental rosettes

Devina Puri[1˚] and Kyle R. Allison[1,2,3*]

[1]*Department of Biomedical Engineering, Emory University and Georgia Institute of Technology, Atlanta, GA*
[2]*Division of Infectious Diseases, Department of Medicine, Emory University School of Medicine, Atlanta, GA*
[3]*Emory Antibiotic Resistance Center, Department of Medicine, Emory University School of Medicine, Atlanta, GA*

*Correspondence: Kyle R. Allison

˚Currently: Department of Molecular Microbiology and Center for Women's Infectious Disease Research, Washington University School of Medicine, Saint Louis, MO

Email: kyle.r.allison@emory.edu

Author Contributions: DP performed experiments and analyses. DP & KRA designed experiments, interpreted results, and wrote the manuscript. KRA developed and performed motility experiments.

Competing Interest Statement: The authors declare no competing interests.

This PDF includes:

Main Text
Figures 1 to 5

Abstract

Rosettes are self-organizing, circular multicellular communities that initiate developmental processes, like organogenesis and embryogenesis, in complex organisms. Their formation results from the active repositioning of adhered sister cells and is thought to distinguish multicellular organisms form unicellular ones. Though common in eukaryotes, this multicellular behavior has not been reported in bacteria. In this study, we discovered that *Escherichia coli* forms rosettes by active sister cell repositioning. After division, sister cells "fold" to actively align at the 2- and 4-cell stages of clonal division, thereby producing rosettes with characteristic quatrefoil configuration. Analysis revealed folding follows an angular random walk, comprised of ~1-µm strokes and directional randomization. We further showed that this motion was produced by the flagellum, the extracellular tail whose rotation generates swimming motility. Rosette formation was found to require *de novo* flagella synthesis suggesting it must balance the opposing forces of *Ag43* adhesion and flagellar propulsion. We went on to show that proper rosette formation was developmentally required for subsequent morphogenesis of multicellular chains, *rpoS* expression, and formation of hydrostatic clonal-chain biofilms. Moreover, we discovered self-folding rosette-like communities in the standard motility assay, indicating this behavior may be general to hydrostatic environments. This study establishes that self-organization of developmental rosettes is a cross-kingdom multicellular behavior. Our findings indicate the potential of targeting bacterial rosettes to interrupt biofilms or reduce their antibiotic tolerance.

41 **Introduction**

42 Multicellularity evolved from unicellular organisms billions of years ago, ultimately producing
43 complex organisms like animals (1). "Multicellularity" is studied in diverse fields, but its meaning
44 can vary from one to another (2). In a basic sense, an organism's multicellularity results from its
45 collected multicellular behaviors, which can range from simple (*e.g.*, cell-cell aggregation) to
46 complicated (*e.g.*, organogenesis). Such behaviors are programmed (3), compared across species
47 (4), experimentally evolved (5), and genetically dissected to understand multicellular development
48 and evolution. Furthermore, identification of shared multicellular behaviors between dissimilar
49 species could point to common design principles of multicellularity.

50 We recently discovered that *Escherichia coli* performs a facultative multicellular life cycle in
51 hydrostatic environments (6, 7) (Fig. S1-2). Though *E. coli*'s relative multicellularity has long
52 been considered (8, 9), our past study established several new multicellular behaviors (6).
53 Tracking how an individual cell creates a multicellular biofilm, we observed the self-assembly of
54 freely-moving multicellular chains (6). These chain communities were clonal, *i.e.* all cells
55 descended form a single parental cell, and grew in length before later attaching to surfaces (6). We
56 demonstrated this self-assembly had sequential morphogenetic stages, each regulated by a specific
57 extracellular adhesin (6). Briefly, the self-recognizing outer-membrane protein Antigen-43 (*Ag43*)
58 maintained sister-cell adhesion and clonality (starting at 2-cell stage); the extracellular polymer
59 type-1 fimbriae controlled chain stability (~8-cell stage); the amyloid-like curli controlled cellular
60 positioning in chains (~16-cell stage); and the extracellular polysaccharide poly-b-1,6-N-acetyl-
61 D-glucosamine (PGA) attached chains to surfaces (~1,000-cell stage) (6). Adapting a standard
62 biofilm assay (7, 10), we showed hydrostatic *E. coli* biofilms resulted from this multicellular
63 pathway (6), supporting the past idea that biofilms represent microbial parallels to *development* in
64 multicellular organisms (11, 12). Several of *E. coli*'s newly-identified behaviors are common to

complex organisms, which also develop through clonally-adhered division (4) and the stabilization of cellular positions by extracellular matrix (ECM) production (13). Additionally, *E. coli* cells were found to align in parallel to form square 4-cell "quatrefoil" communities (6), which we labeled "rosettes" following earlier descriptions of similar communities in mammalian host cells (14, 15). These rosettes partly enclosed an internal space and initiated multicellular morphogenesis (6), similar to developmental rosettes in multicellular organisms.

The rosette motif is ubiquitous in multicellular organisms and represents a key functional unit of tissue morphogenesis (16). Generally, rosettes are self-organizing, circular arrangements of cells that enclose an internal space and initiate developmental processes. They guide development across multiple scales (17), including of embryos (18), organs (19), and neurons (20-22). They are also thought to evolutionarily distinguish multicellular organisms from their unicellular relatives (4), and they are formed by many simple eukaryotes, including *Salpingoeca rosetta* (23), *Chlamydomonas* (24), and human parasites like *Toxoplasma* (25) and *Leishmania* (26). These examples are all flagellates that can perform clonally-adhered division, and *S. rosetta* in particular forms clonal rosettes by flagella-dependent repositioning of sister cells (27). Previously, it has been hypothesized that all animals descend from an ancient flagellate, capable of forming rosette-like communities, and that evolution of alternative repositioning mechanisms may have made the flagellum redundant (4). Hence, clonal rosette formation by cellular repositioning is a fundamental multicellular behavior performed by diverse eukaryotes. By contrast, this behavior has not been reported in bacteria. Though a variety of bacterial communities have been labeled "rosettes" (28-31), their formation is often unclear.

We considered the possibility that *E. coli* might initiate its multicellular life cycle by forming rosettes through cellular repositioning, similar to multicellular eukaryotes. Our past study showed

88 that *Ag43* facilitated cell-cell adherence in rosettes while other adhesins, like fimbriae and curli,
89 did not play a role until after rosette formation (6). However, *Ag43* adhesion alone should result
90 in cells adhered solely at their poles (32) and is insufficient to explain quatrefoil configurations.
91 This raises a potential role for *E. coli*'s flagellum, an extracellular tail that is rotated like a propeller
92 by a molecular motor to produce swimming motility (33, 34). The flagellar motor switches
93 between two rotational directions which separately cause swimming and tumbling, thereby
94 producing a random walk (35, 36). The flagellum is required for hydrostatic biofilm formation,
95 though its control by chemotaxis genes appears dispensable (37, 38). Despite this requirement,
96 there was no evidence of swimming during the multicellular morphogenesis that generated
97 hydrostatic biofilms (6), suggesting an alternative role for the flagellum. An example of flagella-
98 assisted sister cell repositioning in *E. coli* was reported nearly 60 years ago (39) but, evidentally,
99 was not further studied. Though our previous study reported *E. coli* rosettes (6), we did not
100 rigorously investigate them given the incompatible time scales of their formation (minutes or less)
101 and multicellular chain morphogenesis (hours). Here we combine microscopy, genetics, and
102 quantitative analyses to investigate the mechanism and developmental consequences of *E. coli*
103 rosette formation.
104

105 **Results**

106 We used recently-developed methods (6) to record the motion of individual *E. coli* cells (model
107 commensal strain K12 MG1655) by both bright-field and fluorescence microcopy. The resulting
108 videos revealed *E. coli* rosettes form by a consistent behavior (Movies S1-2). Sister cells divided
109 and adhered to each other at their new poles. After ~10 minutes of negligible motion, cells
110 "folded" onto one another, pivoting about their adhered poles to align in parallel (Fig. 1A) similar
111 to previously-described motion (39). This folding often occurred in less than one minute and was

112 comprised of angular movements interspersed with pauses. 2-cell "doublets" then grew and
113 synchronously divided creating 4-cell groups, which folded while keeping their poles in contact to
114 produce quatrefoil rosettes. No additional folding took place after 4-cell rosettes had formed (Fig.
115 1B). Instead, new sister cells adhere at their poles after division and transitioned into
116 longitudinally growing chains while approximately keeping quatrefoil configuration. These
117 findings demonstrate that rosettes are generated by sister-cell folding at the 2-cell and 4-cell stages.
118 Cellular folding, combine with the stabilization of resulting quatrefoil structure by ECM
119 production (6), provides an explanation for the well-defined morphogenesis of *E. coli* multicellular
120 chains.

121 To quantify folding, we next fluorescently imaged cells containing green fluorescent protein
122 to enable image processing (GFP) (Fig. 1C; Fig. S3-8; Movies S3-7) and calculated the 2-
123 dimensional angle between sister cells (θ) (Fig. S9). Changes in θ were small immediately after
124 division, but greatly increased as sister cells folded into parallel orientation (Fig. S9 & 11).
125 Circumferential rotation of cells around their long axis ("spinning") (Movie S3) was also noted
126 during pauses, further indicating folding is a combination of angular movements and paused
127 spinning. We calculated the delay period between cell division and the onset of folding to be ~13
128 minutes (Fig. S11). The maximum angular speed was >6°/s, the detection limit based on the 30-
129 second imaging rate (Fig. S10-11). These findings demonstrate that sister-cell folding is
130 comprised of two distinct motions and is regulated relative to the cell cycle, but also indicate that
131 faster, three-dimensional data will be required.

132 To further quantify sister-cell folding, we recorded bright-field videos at 2-second resolution
133 (Fig. S12-16; Movies S8-12), and tracked the position of cell poles. The angle between a cell and
134 the cover glass (Φ) can be imputed by trigonometry from the cell's length and 2D-projection.

135 Together, θ and Φ values fully specify the 3-dimensional angle between sister cells. Calculated θ
136 dynamics (Fig. 1D; S17) were consistent with the fluorescent data (Fig. S11), revealing delayed-
137 onset sister-cell folding. The cell-averaged maximum angular speed of θ was calculated to be
138 ~36°/s (Fig. S18). Φ dynamics (Fig. S19) were similar to θ dynamics and significant changes in
139 Φ and θ coincided (Fig. 1E; Fig. S20). The angular trajectories of sister cells (plotting Φ against
140 θ) suggested folding may perform an angular random walk (Fig. 1F; Fig. S21). We calculated
141 trajectories of the un-adhered cell poles in Cartesian coordinates, which also suggested random-
142 walk motion (Fig. 1G; Fig. S22-23) and illustrated that folding resulted from switching between
143 angular strokes and paused directional randomization. Inter-stroke pause times fit a long-tail
144 distribution (Fig. S24) with similar time scales to rotational switching of the flagellum (40-42).
145 Stroke distance was 0.8-1.2 μm (Fig. 1H), though in some cells increased to ~2 μm immediately
146 before folding completed. The angle between consecutive strokes (δ) was found to be uncorrelated
147 (r=-0.041; n=59) and near uniformly distributed (Fig. 2I; Fig. S25) satisfying the criteria for a
148 simple random walk (43).

149 Based on this motion and the considerations provided in the introduction, we hypothesized
150 that sister-cell folding was generated by the flagellum (Fig. 2A), and we tracked non-motile Δ*fliC*
151 and Δ*motA* strains (Movies S13-14). Δ*fliC* cells lack the main tail protein while Δ*motA* cells lack
152 a motor component and are deficient in propulsion. Initially, Δ*fliC* and Δ*motA* cells behaved
153 similarly to wild-type: they grew, divided, and adhered at their poles (Fig. 2B & D). However,
154 neither Δ*fliC* nor Δ*motA* cells produced angular movements or folded into rosettes. Instead, Δ*fliC*
155 and Δ*motA* cells grew in linear, unfolded chains where cells were solely adhered to each other at
156 their poles (Fig. 2C & E). Quantifying θ demonstrated negligible angular motion in Δ*fliC* and
157 Δ*motA* cells (Fig. 2F & G). Angular motion at the 2-cell and 4-cell stages in wild-type, and its

158 lack in Δ*fliC* and Δ*motA*, was further demonstrated by quantifying community length, which
159 suddenly halves when sister-cell folding occurs (Fig. 2H; Fig. S26). These findings demonstrate
160 that *E. coli* sister cells reposition themselves into rosettes by flagella propulsion, similar to *S.*
161 *rosetta* (27). Similar mechanisms in the bacterium *E. coli* and eukaryote *S. rosetta* indicate that
162 clonal self-assembly of rosettes by flagella propulsion is a cross-kingdom multicellular behavior.

163 We next sought to elucidate the precise connection between flagella rotation and cellular
164 motion during folding. The flagellum can rotate in both the clockwise (CW) and counterclockwise
165 (CCW) directions, causing tumbling and linear swimming, respectively. We hypothesized that
166 CW and CCW directions produced angular strokes and directional randomization, respectively.
167 To test this, we used Δ*cheY* (mainly CCW) and Δ*cheZ* (mainly CW) mutants (44, 45). Videos
168 demonstrated that the Δ*cheY* mutation abolished angular stokes (Fig. S26-30; Movies S15-17).
169 However, some Δ*cheY* cells "pushed" past each other to align in parallel, though with an opposite
170 polar orientation to folding. This push motion resembled the expected CCW-generated swimming
171 of this strain (44, 45). Quantifying motion of Δ*cheY* sister cells revealed that travel distance
172 remained <0.6 μm (Fig. 2I) and was comparable to the random motion of wild-type cells before
173 they began folding (Fig. 2I, inset). Sister-cell angular trajectories in Δ*cheY* further demonstrated
174 that angular strokes were abolished and illustrated that pushing rather than folding was responsible
175 when parallel alignment did occur (Fig. 2J). We next tracked Δ*cheZ* sister cells and found that this
176 mutation abolished the pauses between angular strokes (Fig. S31-34; Movies S18-20). Moreover,
177 Δ*cheZ* sister cells often forcibly separated, similar to previously-described motion (39), thereby
178 blocking community formation (Fig. S35). Quantifying sister-cell motion and angular trajectories
179 further demonstrated that Δ*cheY* mutation abolished the pauses and caused cell separation (Fig. 2I
180 & K). Together, these findings confirm that CW flagella rotation produces the angular strokes of

181 sister cells while CCW flagella rotation produces their directional randomization. This reflects an
182 inversion of the functional roles of flagella rotation in chemotaxis where CCW causes swimming
183 (directional motion) and CW causes tumbling (directional randomization) (35, 36).

184 Though these findings reveal how flagella rotation produces the motions of sister-cell folding,
185 the role of switching between rotational directions is unclear. CW rotation alone should produce
186 sufficient motion to fully fold sister cells, and CCW should therefore be dispensable. However,
187 when CCW rotation is absent, CW rotation forcibly separates sister cells and blocks rosette
188 formation. Taken together, this may suggest switching itself serves a role in rosette formation,
189 possibly by "braking" the angular motion. Such braking would prevent sister-cell separation and
190 increase the probability of rosette formation in wild-type relative to Δ*cheZ* cells. To explore this,
191 we quantified the frequency of community configurations after several generations (Fig. S36), and
192 found that ~83% of wild-type, ~29% of Δ*cheZ,* ~0% of Δ*cheY* communities were rosettes or
193 rosette-configured chains. The remainder of communities were either single-cell-wide chains or
194 aggregates lacking rosettes configuration. These results indicate that rotational switching itself is
195 important to rosette folding, but not an absolute requirement. In the future, the precise role of
196 motor switching in rosette formation could be determined by controllably varying its rate (40).
197 Moreover, these findings are consistent with past data indicating differences between flagella and
198 chemotaxis genes in hydrostatic biofilm formation (37, 38, 46, 47). It was recently suggested that
199 *E. coli* combines *Ag43* adhesion and AI-2-based chemotaxis to form polyclonal aggregates (46).
200 Our findings do not exclude this possibility, but instead demonstrate that rosettes form by a
201 separate mechanism that also utilizes *Ag43* adhesion and flagellar propulsion.

202 The separation of sister cells by unchecked CW rotation (Δ*cheZ*) suggested flagella propulsion
203 can overcome the adhesive forces holding cells together. Consistently, a role for flagella

204 propulsion in sister cell separation has been described (39). These observations suggest that there
205 may be an optimal amount of force enabling rosette formation. The force produced by a flagellum
206 corresponds to its tail length and number motor subunits (33, 34). Hence, during *de novo* flagella
207 synthesis, it begins at a minimum and increases generations later to strong propulsion by mature
208 flagella (48). We hypothesized that the strong force produced by mature cells would separate sister
209 cells and we investigated this using a motile strain (AW405) that is closely related to MG1655. In
210 AW405, flagellation is repressed by glucose and induced in its absence. This is due to a mutation
211 causing CRP-regulation of the flagella master regulator *flhDC* (49) and allows simple experimental
212 control of flagellation. By fluorescently staining the flagella (50), we confirmed its presence
213 required the absence of glucose (Fig. 3A & B). Next, tracking flagellated AW405 cells in glucose
214 (-) conditions, we observed swimming cells and the separation of all sister cells after division (Fig.
215 3C; Movie S21), consistent with our hypothesis. Even after many generations, no folding, rosettes,
216 or multicellular communities were observed. To verify the flagellum's role, we tracked AW405
217 cells with a Δ*fliC* mutation in glucose (-) conditions and observed sister cells remained adhered at
218 their poles, producing linear, single-cell-wide chains (Fig. 3D; Movie S22) identical to those of
219 MG1655 Δ*fliC* and Δ*motA* cells. In agreement with the Δ*cheZ* data, these findings indicate that
220 strong flagella propulsion separates sister cells and thereby abolishes rosette formation.

221 Adding to the findings in defective-flagella mutants (Δ*fliC* nor Δ*motA*) (Fig. 2), the AW405
222 results suggest rosette formation requires intermediate forces, such as those produced during *de*
223 *novo* flagella biosynthesis (48). Hence, we hypothesized that inducing *de novo* biosynthesis in
224 previously non-flagellated AW405 cells might cause them to self-assemble into rosettes. To test
225 this, we grew AW405 cells in glucose (+) media, transitioned them to glucose (-) to induce flagella
226 biosynthesis, and tracked them by microscopy. In these experiments, sister cells folded at both the

227 2-cell and 4-cell stages, thereby producing quatrefoil rosettes identically to MG1655 (Fig. 3E;
228 Movie S23). This finding indicates that inducing *de novo* flagella biosynthesis is sufficient to
229 enable rosette formation in AW405 and supports the idea that sister cells must balance the
230 opposing forces of adhesion and propulsion to properly reposition into rosettes (Fig. 3F).
231 Balancing of *Ag43*-adhesion and flagella propulsion has been demonstrated in motility assays (51)
232 and could be further characterized by similar studies at the cellular scale.

233 We next sought to investigate the dynamics of flagella biosynthesis during rosette formation.
234 However, methods for flagella staining (50) have not been adapted for real-time tracking of *de*
235 *novo* biosynthesis. Therefore, we characterized the transcriptional dynamics of the flagella
236 pathway using a fluorescent promoter reporter for *fliE* (52), which is directly regulated by *flhDC*
237 and the earliest gene induced during flagella biosynthesis (53). We validated this reporter in
238 AW405 by comparing single-cell *fliE* expression to the number of flagella per cell, which was
239 directly quantified by staining (50) and ranged from 1 to 4 (Fig. S37). We then tracked *fliE*
240 induction dynamics in AW405 cells after transition from glucose (+) to glucose (-) in liquid
241 culture, noting an exponential curve over several generations (Fig. S37). We next tracked *fliE*
242 expression during rosette formation in devices upon transitioning from glucose (+) to glucose (-)
243 as above (Fig. 3E). These experiments demonstrated that *fliE* expression was activated upon
244 switching to glucose (-) and increased exponentially during rosette formation (Fig. 3G). At the
245 time of rosette formation itself, *fliE* expression was between the fluorescence levels corresponding
246 to 0 and 1 flagella per cell, suggesting an intermediate degree of flagella biosynthesis. At
247 approximately the 16-cell stage, *fliE* expression plateaued at a fluorescence level corresponding to
248 1 flagella per cell (Fig. S37). In AW405, individual swimming cells separated from multicellular
249 chains at later time points (~32 cells). This behavior had not been observed in wild-type MG1655,

250 and may result from the more robust activation of flagella biosynthesis in the AW405 strain.
251 Together, these findings demonstrate that transcription of the flagella biosynthesis pathway is
252 induced during rosette formation. Furthermore, the intermediate *fliE* activation suggests folding
253 of rosette corresponds to intermediate flagella biosynthesis, and therefore force. In the future, the
254 development of new real-time staining methods could enable more direct investigation of the
255 flagellum's role in rosette formation.

256 Though we had previously identified rosettes in *E. coli*'s multicellular life cycle (6), it was
257 unclear if they were developmentally required for the subsequent morphogenetic stages. To test
258 this idea we tracked wild-type, Δ*fliC*, and Δ*motA* communities long-term. We found that, even
259 after many generations, both Δ*fliC* and Δ*motA* communities remained linear with cells adhered to
260 one another at their poles (Fig. 4B, & Fig. S38-39) and did not display the well-regulated post-
261 rosette morphogenesis of wild type (Fig. 4A) (6). In contrast to the stable organization of wild-
262 type chains, Δ*fliC* and Δ*motA* communities were unstable and dissociated into smaller groups and
263 individual cells, reminiscent of cells defective in type-1 fimbriae or curli (6). Moreover, Δ*fliC*
264 and Δ*motA* communities poorly attached to cover glass (Fig. S38-39; Movie S24), reminiscent of
265 PGA-defective cells (6). These results show that disabling rosette formation impairs subsequent
266 morphogenetic stages. To gain additional insights into the developmental consequences of rosette
267 formation, we tracked the expression of the alternate sigma factor σ^{38} (encoded by *rpoS*) during
268 chain morphogenesis using a fluorescent promoter reporter (52). σ^{38} is a transcriptional master
269 regulator and controls a variety of genes in biofilms, including those involved in stress tolerance
270 and metabolism (54). We found that *rpoS* expression was strongly induced in wild-type chains
271 between the ~200-cell and ~1000-cell stages prior to surface attachment (Fig. 4C). Despite
272 identical growth conditions, rosette-disabled Δ*fliC* communities did induce *rpoS* expression (Fig.

273 4C). Together, these findings indicate that rosette formation is a developmental requirement for
274 *E. coli*'s facultative multicellular life cycle, and may also be critical to biofilm formation.
275 We have previously shown that *E. coli*'s rosette-initiated chain morphogenesis generates
276 hydrostatic biofilms (6). Hence, we hypothesized that Δ*fliC* and Δ*motA* mutants, which disable
277 rosette formation, would reduce surface attachment and disrupt the clonal-chain architecture of *E.*
278 *coli* biofilms (6). To test this, we grew hydrostatic wild-type, Δ*fliC*, and Δ*motA* biofilms and
279 imaged them at the cellular scale (7). Consistent with our hypothesis, these mutations reduced
280 biofilm volume and abolished the parallel-aligned, clonal-chain structure of wild-type biofilms
281 (Fig. 4D-F). Moreover, Δ*fliC* and Δ*motA* biofilms contained short unfolded chains of cells adhered
282 at their, structurally consistent with the lack of flagella propulsion and rosette formation. These
283 findings further demonstrate the developmental consequences of rosette formation and provide a
284 new rationale for the requirement of flagella to hydrostatic *E. coli* biofilms (37, 38).
285 We next considered that flagella-assisted rosette formation might be general in hydrostatic
286 environments. Aside from biofilm assays, hydrostatic conditions are commonly studied at bulk-
287 scale in motility assays (55, 56). The "swimming agar" used in such assays (~0.2-0.3% agar)
288 provides cells sufficient freedom of motion to swim across the surface. On the other hand, "colony
289 agar" (e.g., >1.5% agar for many species) limits free motion and forces growth within localized
290 colonies. We reasoned that, if rosette formation was general to hydrostatic environments, then we
291 should observe them during *E. coli* growth on swimming agar. Conducting standard motility
292 assays (51, 57) and imaging after ~2 hours, we observed freely-moving rosette-like communities
293 and multicellular chains in the regions where cells had been initially deposited, suggesting rosette
294 formation can occur on swimming agar (Fig. 4G; Movies S25-27). In these experiments, we also
295 observed examples of cellular folding in real time (Movies S28-29). To investigate the mechanism

296 of community folding on swimming agar, we performed similar experiments with Δ*fliC* and Δ*flu*
297 (*Ag43*) strains. We observed that Δ*fliC* cells were mostly adhered at the poles in linear, unfolded
298 chains, demonstrating the flagellum is required for folding on swimming agar (Fig. 4H; Movie
299 S30). Moreover, Δ*flu* cells were predominately individuals and were rarely observed in aggregates
300 (Fig. 4I; Movie S31). These findings are in agreement with a previous study demonstrating
301 balancing between *Ag43* adhesion and flagella propulsion on motility plates (51). Moreover, they
302 indicate the formation of rosettes on swimming agar and the requirement for *Ag43* adhesion and
303 flagella propulsion. Additionally, the imaging technique we have developed could be optimized
304 and extended to further investigate the genetics and dynamics of bacterial multicellular behavior
305 in hydrostatic environments.
306

307 **Discussion**

308 This study has revealed *E. coli* forms rosettes by a simple mechanism, flagella-assisted
309 repositioning of sister cells. Flagella propulsion produces an angular random walk between sister
310 cells (Fig. 1-3), thereby folding them in parallel alignment at the 2- and 4-cell stages (Fig. 1). The
311 synchronization of cell division events further explains the robustness of quatrefoil rosettes and
312 why alternatives like 3-, 5-, or 6-cell rosettes were not observed. We demonstrated that rosettes
313 are required for subsequent morphogenesis of multicellular chains, *rpoS* expression, and formation
314 of clonal-chain biofilms (Fig. 4). Consistent findings were made in diverse experimental
315 conditions, including devices (Fig. 1-3), biofilms (Fig. 4), and swimming agar (Fig. 4), suggesting
316 that rosette formation may be a general behavior in hydrostatic environments and has a straight-
317 forward dependence on mechanical constraints. The small forces produced by mature flagella are
318 sufficient to separate sister cells (Fig. 3), indicating bulk-scale forces, like mechanical shaking for
319 culture agitation, would necessarily block rosette formation and would thereby effectively explain

320 why fluid flow impairs commensal *E. coli* biofilm formation (58). On the other hand, forcing cells
321 against surfaces, such as colony growth on agar or on cover glass in flow cells, constrains cell
322 motion and blocks repositioning into rosettes. Mechanically speaking, hydrostatic conditions
323 would then be necessary for commensal *E. coli* rosette formation and subsequent biofilm
324 morphogenesis.

325 This study also updates *E. coli*'s facultative multicellular life cycle (6), which has now
326 provided roles for many of the genes required for hydrostatic biofilm formation (38). Adding to
327 those outlined in the introduction, our current findings revealed new multicellular behaviors:
328 induction of flagella biosynthesis at the 2-cell stage leads to cellular repositioning at the 2- and 4-
329 cell stages to produce rosettes; and expression of *rpoS* is induced at ~200-cell stage. The active
330 mechanism of rosette formation and its requirement for subsequent multicellular behaviors further
331 support the idea that *E. coli*'s facultative life cycle is an organized developmental process with
332 regulated stages (illustrated in Fig. 5). In the future, the generative structural interactions could be
333 further validated by new real-time staining techniques. This pathway may be specific to *E. coli,*
334 perhaps reflecting its natural habitats, but other bacteria perform similar phenomena. *Bacillus*
335 *subtilis*, for example, can produce biofilms by multicellular chain morphogenesis (59) which is
336 maintained by ECM production (60) and has genetically-regulated stages (61), though rosettes
337 have not been reported. As reported here, *E. coli*'s mechanism of rosette formation is currently
338 unique as the rosettes described in other species either propagate through binary fission (31) or
339 result from the entanglement of flagella without enclosing an internal space (28-30).

340 Moreover, this study is the first report of clonal rosette formation by cellular repositioning in
341 bacteria. In principle, the same behavior underlies simple eukaryotic multicellularity and is
342 hypothesized as a key step in the evolution of complex organisms (4). Similar to *E. coli*, *S. rosetta*

343 cells with mature flagella separate and those lacking flagella adhere in unfolded linear chains (23).
344 Hence, our study demonstrates that clonal self-organization of developmental rosettes is a cross-
345 kingdom behavior and may represent a common design principle of multicellularity, irrespective
346 of an organism's genomic complexity or evolutionary history. In turn, this principle suggests
347 rosette self-assembly might provide a foundational stage for programming synthetic multicellular
348 behaviors, a goal for *E. coli* (62) since early on in synthetic biology (63, 64). Though *E. coli* lacks
349 complexity relative to even the simplest eukaryotes, rosette formation may provide a basis for
350 engineering or evolving increasingly complex behavior in a tractable unicellular organism.

351 This study additionally suggests rosettes might be targeted to control *E. coli*'s natural
352 multicellular behaviors, including the formation of biofilms. Hydrostatic biofilms depend on
353 rosette formation (Fig. 4) which in turn relies on the balance of sister-cell adhesion and flagella
354 propulsion (Fig. 3). Tuning this balance could potentially be used to modulate the biofilm capacity
355 of commensal *E. coli* strains, which form multicellular communities (65) in the ~1 mm-thick
356 intestinal mucosa (66) as members of the microbiome (67). Alternatively, flagella motion could
357 be blocked to therapeutically inhibit *E. coli* biofilms, which contribute to urinary-tract infections
358 (68) and are highly tolerant to antibiotics (69). This tolerance depends on expression of biofilm-
359 related genes, including those regulated by *rpoS* (70). Hence, as rosettes are critical to adaptive
360 gene expression (Fig. 4), disrupting their formation might also enhance antibiotic susceptibility.
361 Such rosette-targeting approaches could be combined with newly-discovered antibiotics (71-73)
362 or complement mechanism-based improvement of existing antibiotics (74, 75), such as the
363 metabolic potentiation of aminoglycosides (76-79).

364 ## Materials and Methods

365 **Strains, Plasmids, and Media**

366 *Escherichia coli* MG1655 was the primary strain used in experiments. *E. coli* AW405 strains were
367 also used where specified. To facilitate computational image processing and analysis and also
368 biofilm imaging, *E. coli* cells were transformed with pUA66-p*ompC*::*gfp* (green) (52) or pEB2-
369 mScarlet (red) (80). These plasmids constitutively express fluorescent proteins and had no
370 observable effects on cellular behaviors. Additionally, pUA66-p*fliE*::*gfp* and pUA66-p*rpoS*::*gfp*
371 (52) were also transformed into MG1655 and studied where described. The Δ*fliC*, Δ*motA*, Δ*cheZ*,
372 Δ*cheY*, and Δ*flu* strains were created by transducing Δ*fliC*::kan(kanR), Δ*motA*::kan(kanR),
373 Δ*cheZ*::kan(kanR), Δ*cheY*::kan(kanR), and Δ*flu*::kan(kanR) respectively from the KEIO
374 Collection (81) using *P1vir* in *E. coli* MG1655 following standard methods (82), and were cured
375 with pCP20 (83). All strains were cultured in LB, Miller broth (Difco) at 37°C and with shaking
376 at 300 RPM, in 14 mL Falcon Round-Bottom Test Tubes with aerating caps (VWR), and in light-
377 insulated shakers. LB lacks significant glucose and was therefore used as a glucose (-) condition.
378 Glucose (+) experiments used Neidhardt Supplemented MOPS Defined Medium (EZ-rich;
379 Teknova) (84). When necessary, plasmids were maintained by supplementing media with 50
380 μg/mL of kanamycin.

381

382 **Cell Tracking in Hydrostatic Devices**

383 LB agarose pad devices were built using 2% agarose, following previously described methods (6).
384 3 μL exponential phase cells were added to agarose pads, which were immediately covered with
385 cover glass without allowing them to dry. This generated a liquid space ~0.75 cm x 0.75 cm that
386 we approximated as ~5-10 μm deep based on the distance between the focal planes of the cover

387 glass and agarose. These devices were developed to allow observation of the free motion of cells
388 in a hydrostatic environment. For glucose transition experiments, *E. coli* AW405 cells were first
389 cultured overnight in Neidhardt Supplemented MOPS Defined Medium (EZ-rich; Teknova) and
390 then loaded onto LB-2% agarose pads for cell tracking. Dynamic bright-field imaging was
391 typically conducted at 2-second resolution. Dynamical fluorescent imaging for motion tracking
392 was performed at 30-second resolution (instead of 2-second) to avoid the confounding effects of
393 exposing bacteria to high-intensity blue light. Imaging for fluorescent reporters (pUA66-p*fliE*::*gfp*
394 and pUA66-p*rpoS*::*gfp*) was less frequent to reduce photo-bleaching and is specified in legends.
395

396 **Biofilm Imaging**

397 Biofilm experiments were performed as previously described (6, 7). Wells in 96-well plates were
398 loaded with 200 mL of fresh LB with overnight cultured cells (~10^8 CFU/mL). Cultures were a
399 1:10 mixture of cells containing pUA66-p*ompC*::*gfp* (green) and pEB2-mScarlet (red). Cover
400 glass pieces were placed in each well, perpendicular to the air-liquid interface in order to allow for
401 biofilm formation. Plates were then incubated without shaking at 37˚C for 16 hours to allow
402 biofilm formation to occur. After incubation, cover glass pieces were removed from the wells and
403 placed between a glass slide and a fresh piece of cover glass in order to image by microscopy.
404 This method allows high-magnification imaging of hydrostatic biofilms grown following a
405 standard protocol (10).
406

407 **Motility Assay Imaging**

408 Swimming agar is fragile and difficult to remove from a petri dish without damage. To enable
409 handling of swimming agar, we created two layer plates by adapting standard procedures (57).

410 The bottom layer was made from 2% agar and provided a stable base for a top layer of 0.25%
411 swimming agar. This ensured cells spotted on these plates would encounter an identical
412 hydrostatic surface as in classical motility assays and would also have the same environmental
413 nutrients concentrations. We confirmed comparable bulk-scale motility on 2-layer (2% and 0.25%
414 agar) plates and classical swimming agar plates (0.25 % agar) by incubation for 18 hours at 37˚C
415 (Fig. S40) following previous methods (51). For imaging directly on motility plates, we first
416 poured a 12 mL layer of molten 2% LB agar in petri dishes and allowed them to cool overnight.
417 The day of motility experiments, we poured 8 mL of molten 0.25% LB agar (at 50˚C) on top of
418 the 2% layer and cooled. 2-layer plates were pre-warmed at 37˚C, then 10 μL of exponentially
419 growing cell suspensions diluted to ~10^5-10^6 CFU/mL were spotted in the middle. Plates were
420 then incubated face up for 1-2 hours at 37˚C. After incubation, a ~1 cm x 1 cm square containing
421 the location of the initial 10 μL spot was cut in the agar using a scalpel. The remaining agar was
422 removed from around this square. Cover glass was placed on top of this square, resting on the
423 hydrostatic surface of the swimming agar. Immersion oil was added to the cover glass, then the
424 agar and cover glass were carefully inverted and placed directly in a microscope sample holder
425 and immediately imaged. As cells and communities were in motion, capturing them required
426 recording videos in bright-field DIC.
427
428 **Microscopy**
429 Images were acquired using a Leica DMi8 microscope equipped with a DIC HCPL APO 63X oil
430 immersion objective (with 1.6x magnification changer), Hamamatsu ORCA-Flash 4.0 camera, and
431 Lumencor Spectra-X light engine. Devices for imaging were secured in a microscope-stage-top
432 incubator (Tokai-Hit, STX Stage Top Incubator Temp and Flow; STXF-WSKMX-SET), and the
433 incubator and the microscope objective were maintained at 37˚C prior to and throughout all

experiments. Time courses were collected in an automated manner using the Leica LasX software at specified time intervals. Imaging was performed using differential interference contrast (DIC) and fluorescence channels. Excitation and emission for fluorescence microscopy was performed at 470 nm and 500-550 nm for green fluorescence and 510 nm and 592-668 nm for red fluorescence respectively. AW405 flagella were stained as previously described (50) with Alexa Fluor 488. Micrograph examples and movies were generated using Leica X software.

Image Analysis

Fluorescent images of cells were analyzed using built-in Matlab functions. Briefly, raw images were cropped to include only one sister-cell pair or multicellular community then were segmented using the *imbinarize* function. Centerlines of cells were then determined using the *bwskel* function and used to calculate the angle θ between sister cells. *imbinarize* was also used for the transcriptional reporter data (*fliE* and *rpoS*), and the average pixel intensity of the segmented area was calculated to determine cellular fluorescence. Bright-field DIC images of cells were first processed in ImageJ to manually mark the poles for both the sister cells. Coordinates for these pole positions were then loaded into MATLAB for calculating motion. θ was determined as the 2D angle created by the pole positions of two sister cells, and these values were also used to determine the angular velocity. Φ represented the angle between a cell and the imaging surface, in the z direction (toward the camera). This was imputed by trigonometry from the calculated length of the 2-D projection of the cell (the xy distance between a cell's two poles when it was at an angle to the xy plane) and its calculated maximum length immediately prior to folding. As folding occurred within seconds, negligible cell growth (which has a doubling time ~30 minutes) occurs, and cell length was treated as constant when calculating Φ. Strokes were identified as motion between consecutive 2-second images that exceeded 0.8 μm. δ was defined as the angle

458 in 3D space between the vectors created by two consecutive strokes. Figures were generated in
459 Matlab and arranged and formatted using Adobe Illustrator.
460

461 **Replicates and Statistical Analysis**

462 Each replicate corresponds to an independent sister-cell pair or chain community, tracked over
463 time. Replicates were chosen as representative examples from 3 or more separate experiments,
464 and their number (n) is listed in figure legends. Mean and standard deviations are calculated where
465 indicated. Micrographs and images are representative examples from replicated experiments.
466

467 **Acknowledgements**

468 We are grateful to Howard C. Berg and Karen Fahrner for sharing AW405 strains and Philippe
469 Cluzel for sharing pEB2-mScarlet. This study was supported by an NIH Director's Early
470 Independence Award (DP5OD019792) to Kyle R. Allison.

References

1. Knoll AH (2011) The Multiple Origins of Complex Multicellularity. *Annu Rev Earth Pl Sc* 39:217-239.
2. Rose CJ & Hammerschmidt K (2021) What Do We Mean by Multicellularity? The Evolutionary Transitions Framework Provides Answers. *Front Ecol Evol* 9.
3. Toda S, Blauch LR, Tang SKY, Morsut L, & Lim WA (2018) Programming self-organizing multicellular structures with synthetic cell-cell signaling. *Science* 361(6398):156-162.
4. Brunet T & King N (2017) The Origin of Animal Multicellularity and Cell Differentiation. *Dev Cell* 43(2):124-140.
5. Ratcliff WC, Denison RF, Borrello M, & Travisano M (2012) Experimental evolution of multicellularity. *P Natl Acad Sci USA* 109(5):1595-1600.
6. Puri D, Fang X, & Allison KR (2023) Evidence of a possible multicellular life cycle in Escherichia coli. *iScience* 26(1):105795.
7. Puri D, Fang X, & Allison KR (2023) Fluorescence-based protocol for revealing cellular arrangement in biofilms. *STAR Protoc* 4(2):102270.
8. Shapiro JA (1998) Thinking about bacterial populations as multicellular organisms. *Annual Review of Microbiology* 52:81-104.
9. Shapiro JA (1988) Bacteria as Multicellular Organisms. *Sci Am* 258(6):82-89.
10. O'Toole GA (2011) Microtiter dish biofilm formation assay. *J Vis Exp* (47).
11. Monds RD & O'Toole GA (2009) The developmental model of microbial biofilms: ten years of a paradigm up for review. *Trends Microbiol* 17(2):73-87.
12. O'Toole G, Kaplan HB, & Kolter R (2000) Biofilm formation as microbial development. *Annu Rev Microbiol* 54:49-79.
13. Datta A, Bryant DM, & Mostov KE (2011) Molecular regulation of lumen morphogenesis. *Curr Biol* 21(3):R126-136.
14. Justice SS*, et al.* (2004) Differentiation and developmental pathways of uropathogenic Escherichia coli in urinary tract pathogenesis. *Proc Natl Acad Sci U S A* 101(5):1333-1338.
15. Mysorekar IU & Hultgren SJ (2006) Mechanisms of uropathogenic Escherichia coli persistence and eradication from the urinary tract. *Proc Natl Acad Sci U S A* 103(38):14170-14175.
16. Blankenship JT, Backovic ST, Sanny JS, Weitz O, & Zallen JA (2006) Multicellular rosette formation links planar cell polarity to tissue morphogenesis. *Dev Cell* 11(4):459-470.
17. Moran HR & Mosimann C (2023) Rosettes guide the way for mesodermal MET. *Dev Cell* 58(11):917-918.
18. Bedzhov I & Zernicka-Goetz M (2014) Self-organizing properties of mouse pluripotent cells initiate morphogenesis upon implantation. *Cell* 156(5):1032-1044.
19. Bryant DM*, et al.* (2010) A molecular network for de novo generation of the apical surface and lumen. *Nat Cell Biol* 12(11):1035-1045.
20. Wilson PG & Stice SS (2006) Development and differentiation of neural rosettes derived from human embryonic stem cells. *Stem Cell Rev* 2(1):67-77.
21. Hribkova H, Grabiec M, Klemova D, Slaninova I, & Sun YM (2018) Calcium signaling mediates five types of cell morphological changes to form neural rosettes. *J Cell Sci* 131(3).
22. Fan L, Kovacevic I, Heiman MG, & Bao Z (2019) A multicellular rosette-mediated collective dendrite extension. *Elife* 8.
23. Larson BT*, et al.* (2020) Biophysical principles of choanoflagellate self-organization. *Proc Natl Acad Sci U S A* 117(3):1303-1311.
24. Short MB*, et al.* (2006) Flows driven by flagella of multicellular organisms enhance long-range molecular transport. *Proc Natl Acad Sci U S A* 103(22):8315-8319.

518 25. Degrandi D*, et al.* (2013) Murine guanylate binding protein 2 (mGBP2) controls Toxoplasma
519 gondii replication. *Proc Natl Acad Sci U S A* 110(1):294-299.
520 26. Iovannisci DM, Plested CP, & Moe GR (2010) Evidence for rosettes as an unrecognized stage in
521 the life cycle of Leishmania parasites. *J Eukaryot Microbiol* 57(5):405-414.
522 27. Dayel MJ*, et al.* (2011) Cell differentiation and morphogenesis in the colony-forming
523 choanoflagellate Salpingoeca rosetta. *Dev Biol* 357(1):73-82.
524 28. Moore RL & Marshall KC (1981) Attachment and rosette formation by hyphomicrobia. *Appl*
525 *Environ Microbiol* 42(5):751-757.
526 29. Zeng Y & Liu B (2020) Self-propelling and rolling of a sessile-motile aggregate of the bacterium.
527 *Commun Biol* 3(1).
528 30. Ong CJ, Wong ML, & Smit J (1990) Attachment of the adhesive holdfast organelle to the cellular
529 stalk of Caulobacter crescentus. *J Bacteriol* 172(3):1448-1456.
530 31. Keim CN*, et al.* (2004) Multicellular life cycle of magnetotactic prokaryotes. *FEMS Microbiol Lett*
531 240(2):203-208.
532 32. Vejborg RM & Klemm P (2009) Cellular chain formation in Escherichia coli biofilms. *Microbiology*
533 *(Reading)* 155(Pt 5):1407-1417.
534 33. Berg HC (2003) The rotary motor of bacterial flagella. *Annu Rev Biochem* 72:19-54.
535 34. Macnab RM (2003) How bacteria assemble flagella. *Annu Rev Microbiol* 57:77-100.
536 35. Berg HC (1984) (Princeton University Press, Princeton).
537 36. Berg HC (2004) (Springer New York, New York, NY).
538 37. Pratt LA & Kolter R (1998) Genetic analysis of Escherichia coli biofilm formation: Roles of flagella,
539 motility, chemotaxis and type I pili. *Molecular Microbiology* 30(2):285-293.
540 38. Niba ET, Naka Y, Nagase M, Mori H, & Kitakawa M (2007) A genome-wide approach to identify
541 the genes involved in biofilm formation in E. coli. *DNA Res* 14(6):237-246.
542 39. Quesnel LB (1966) Flagella-Assisted Cell Fission in Escherichia Coli. *Nature* 211(5049):659-&.
543 40. Alon U, Surette MG, Barkai N, & Leibler S (1999) Robustness in bacterial chemotaxis. *Nature*
544 397(6715):168-171.
545 41. Korobkova E, Emonet T, Vilar JM, Shimizu TS, & Cluzel P (2004) From molecular noise to
546 behavioural variability in a single bacterium. *Nature* 428(6982):574-578.
547 42. Korobkova EA, Emonet T, Park H, & Cluzel P (2006) Hidden stochastic nature of a single bacterial
548 motor. *Phys Rev Lett* 96(5):058105.
549 43. Codling EA, Plank MJ, & Benhamou S (2008) Random walk models in biology. *J R Soc Interface*
550 5(25):813-834.
551 44. Parkinson JS (1978) Complementation analysis and deletion mapping of Escherichia coli mutants
552 defective in chemotaxis. *J Bacteriol* 135(1):45-53.
553 45. Parkinson JS, Parker SR, Talbert PB, & Houts SE (1983) Interactions between chemotaxis genes
554 and flagellar genes in Escherichia coli. *J Bacteriol* 155(1):265-274.
555 46. Laganenka L, Colin R, & Sourjik V (2016) Chemotaxis towards autoinducer 2 mediates
556 autoaggregation in Escherichia coli. *Nat Commun* 7:12984.
557 47. Suchanek VM*, et al.* (2020) Chemotaxis and cyclic-di-GMP signalling control surface attachment
558 of Escherichia coli. *Mol Microbiol* 113(4):728-739.
559 48. Pruss BM & Matsumura P (1997) Cell cycle regulation of flagellar genes. *J Bacteriol*
560 179(17):5602-5604.
561 49. Fahrner KA & Berg HC (2015) Mutations That Stimulate flhDC Expression in Escherichia coli K-12.
562 *J Bacteriol* 197(19):3087-3096.
563 50. Turner L, Ryu WS, & Berg HC (2000) Real-time imaging of fluorescent flagellar filaments. *J*
564 *Bacteriol* 182(10):2793-2801.

565 51. Ulett GC, Webb RI, & Schembri MA (2006) Antigen-43-mediated autoaggregation impairs
566 motility in Escherichia coli. *Microbiology (Reading)* 152(Pt 7):2101-2110.
567 52. Zaslaver A*, et al.* (2006) A comprehensive library of fluorescent transcriptional reporters for
568 Escherichia coli. *Nature Methods*.
569 53. Kalir S*, et al.* (2001) Ordering genes in a flagella pathway by analysis of expression kinetics from
570 living bacteria. *Science* 292(5524):2080-2083.
571 54. Battesti A, Majdalani N, & Gottesman S (2011) The RpoS-mediated general stress response in
572 Escherichia coli. *Annu Rev Microbiol* 65:189-213.
573 55. Harshey RM (2003) Bacterial motility on a surface: many ways to a common goal. *Annu Rev*
574 *Microbiol* 57:249-273.
575 56. Girgis HS, Liu YC, Ryu WS, & Tavazoie S (2007) A comprehensive genetic characterization of
576 bacterial motility. *Plos Genet* 3(9):1644-1660.
577 57. Kearns DB (2010) A field guide to bacterial swarming motility. *Nat Rev Microbiol* 8(9):634-644.
578 58. Schembri MA & Klemm P (2001) Biofilm formation in a hydrodynamic environment by novel
579 FimH variants and ramifications for virulence. *Infection and Immunity*.
580 59. Branda SS, Gonzalez-Pastor JE, Ben-Yehuda S, Losick R, & Kolter R (2001) Fruiting body
581 formation by Bacillus subtilis. *Proc Natl Acad Sci U S A* 98(20):11621-11626.
582 60. van Gestel J, Vlamakis H, & Kolter R (2015) Division of Labor in Biofilms: the Ecology of Cell
583 Differentiation. *Microbiol Spectr* 3(2):MB-0002-2014.
584 61. Kobayashi K (2007) Bacillus subtilis pellicle formation proceeds through genetically defined
585 morphological changes. *J Bacteriol* 189(13):4920-4931.
586 62. Basu S, Gerchman Y, Collins CH, Arnold FH, & Weiss R (2005) A synthetic multicellular system for
587 programmed pattern formation. *Nature* 434(7037):1130-1134.
588 63. Gardner TS, Cantor CR, & Collins JJ (2000) Construction of a genetic toggle switch in Escherichia
589 coli. *Nature* 403(6767):339-342.
590 64. Elowitz MB & Leibler S (2000) A synthetic oscillatory network of transcriptional regulators.
591 *Nature* 403(6767):335-338.
592 65. Rossi E*, et al.* (2018) "It's a gut feeling" - biofilm formation in the gastrointestinal tract
593 environment. *Crit Rev Microbiol* 44(1):1-30.
594 66. Atuma C, Strugala V, Allen A, & Holm L (2001) The adherent gastrointestinal mucus gel layer:
595 thickness and physical state in vivo. *Am J Physiol Gastrointest Liver Physiol* 280(5):G922-929.
596 67. Tenaillon O, Skurnik D, Picard B, & Denamur E (2010) The population genetics of commensal
597 Escherichia coli. *Nat Rev Microbiol* 8(3):207-217.
598 68. Anderson GG*, et al.* (2003) Intracellular bacterial biofilm-like pods in urinary tract infections.
599 *Science* 301(5629):105-107.
600 69. Yan J & Bassler BL (2019) Surviving as a Community: Antibiotic Tolerance and Persistence in
601 Bacterial Biofilms. *Cell Host Microbe* 26(1):15-21.
602 70. Ito A, Taniuchi A, May T, Kawata K, & Okabe S (2009) Increased antibiotic resistance of
603 Escherichia coli in mature biofilms. *Appl Environ Microbiol* 75(12):4093-4100.
604 71. Stokes JM*, et al.* (2020) A Deep Learning Approach to Antibiotic Discovery. *Cell* 180(4):688-702
605 e613.
606 72. Martin JK, 2nd*, et al.* (2020) A Dual-Mechanism Antibiotic Kills Gram-Negative Bacteria and
607 Avoids Drug Resistance. *Cell* 181(7):1518-1532 e1514.
608 73. Imai Y*, et al.* (2019) A new antibiotic selectively kills Gram-negative pathogens. *Nature*
609 576(7787):459-464.
610 74. Allison KR, Brynildsen MP, & Collins JJ (2011) Heterogeneous bacterial persisters and
611 engineering approaches to eliminate them. *Curr Opin Microbiol* 14(5):593-598.

612 75. Fang X & Allison KR (2023) Resuscitation dynamics reveal persister partitioning after antibiotic
613 treatment. *Mol Syst Biol* 19(4):e11320.
614 76. Allison KR, Brynildsen MP, & Collins JJ (2011) Metabolite-enabled eradication of bacterial
615 persisters by aminoglycosides. *Nature* 473(7346):216-220.
616 77. Rosenberg CR, Fang X, & Allison KR (2020) Potentiating aminoglycoside antibiotics to reduce
617 their toxic side effects. *PLoS One* 15(9):e0237948.
618 78. Barraud N, Buson A, Jarolimek W, & Rice SA (2013) Mannitol enhances antibiotic sensitivity of
619 persister bacteria in Pseudomonas aeruginosa biofilms. *PLoS One* 8(12):e84220.
620 79. Meylan S*, et al.* (2017) Carbon Sources Tune Antibiotic Susceptibility in Pseudomonas
621 aeruginosa via Tricarboxylic Acid Cycle Control. *Cell Chem Biol* 24(2):195-206.
622 80. Balleza E, Kim JM, & Cluzel P (2018) Systematic characterization of maturation time of
623 fluorescent proteins in living cells. *Nature Methods* 15(1):47-51.
624 81. Baba T*, et al.* (2006) Construction of Escherichia coli K-12 in-frame, single-gene knockout
625 mutants: The Keio collection. *Molecular Systems Biology* 2.
626 82. Thomason LC, Costantino N, & Court DL (2007) E. coli Genome Manipulation by P1
627 Transduction.), pp 1.17.11-11.17.18.
628 83. Datsenko KA & Wanner BL (2000) One-step inactivation of chromosomal genes in Escherichia
629 coli K-12 using PCR products. *Proc Natl Acad Sci U S A* 97(12):6640-6645.
630 84. Neidhardt FC, Bloch PL, & Smith DF (1974) Culture medium for enterobacteria. *J Bacteriol*
631 119(3):736-747.

632

Figures

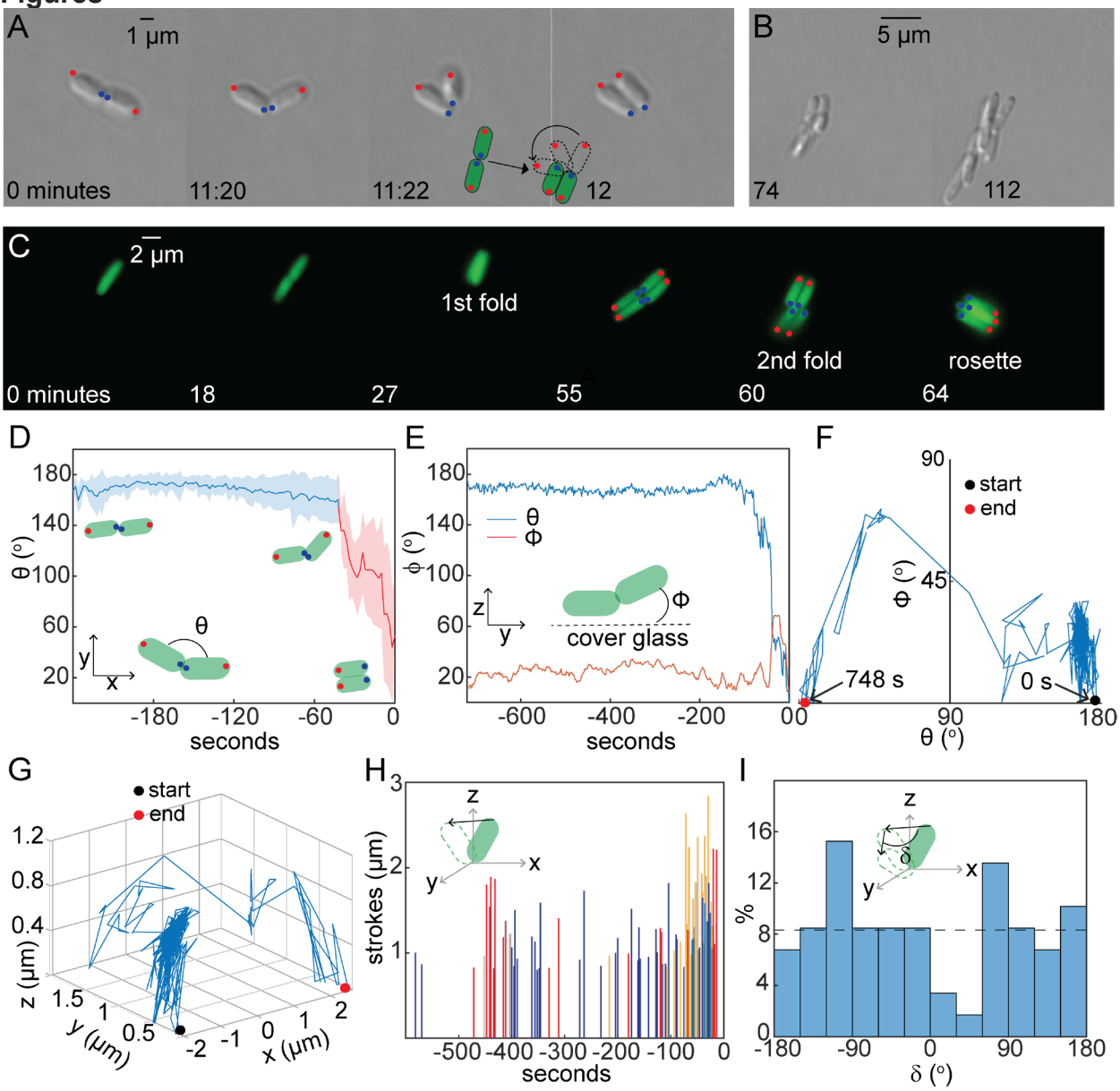

Figure 1. Sister-cell folding produces rosettes and follows an angular random walk. (A) Micrographs from a representative movie (2-second resolution) of *E. coli* sister-cell folding and parallel alignment. Time and scale indicated on all micrographs. New (blue) and old (red) poles are indicated. Inset: illustration of cell folding documented in movies. (B) Later micrographs from the same video. (C) Micrographs from a representative movie (30-second resolution) of rosette formation in cells constitutively-expressing GFP. New (blue) and old (red) poles are indicated. (D) Dynamics of sister-cell angle (θ) during cellular folding (2-second resolution; mean ± standard

642 deviation, n=5). Folding (red) and pre-folding (blue) are indicated. Inset: illustration of θ
643 calculation. (E) Representative example of sister cell θ (blue) and Φ (red). Inset: illustration of Φ
644 calculation. (F) Trajectory of sister-cell angles from representative example of folding. Start and
645 end positions and times are indicated. (G) Representative example of 3D trajectory of cell pole
646 during folding. (H) Dynamics of angular strokes (movement >0.8 μm) for 4 representative sister-
647 cell pairs. Inset: illustration of distance calculation. (I) Distribution of angle change between
648 strokes (δ) (59 recorded strokes across 5 independent sister cell pairs). Inset: illustration of δ
649 calculation.

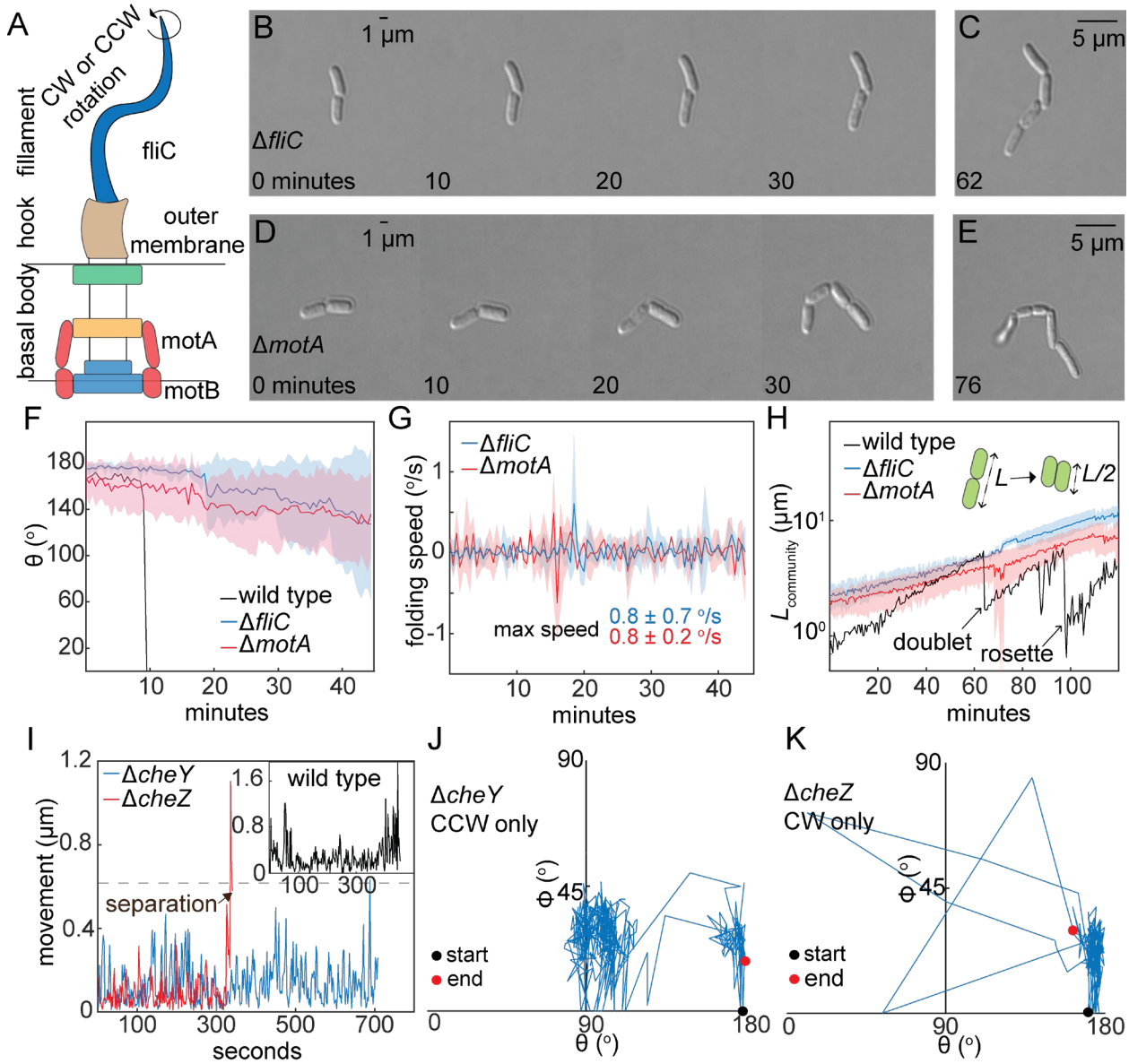

Figure 2. Flagella propulsion generates sister cell folding. (A) Diagram of the flagellum (not to scale). Micrographs from representative movies of (B) Δ*fliC* and (D) Δ*motA* cells. Time and scale indicated on all micrographs. Later micrographs of (C) Δ*fliC* and (E) Δ*motA* cells from the same videos. (F) Dynamics of Δ*fliC* (blue) and Δ*motA* (red) sister-cell angle (30-second resolution; mean ± standard deviation, n=3). An example wild-type trajectory is included for comparison. (G) Dynamics of angular speed for Δ*fliC* and Δ*motA* cells (30-second resolution; mean ± standard deviation, n=3). Inset: average maximum speed during. (H) Length dynamics of Δ*fliC* and Δ*motA*

658 communities (mean ± standard deviation; n= 3). An example wild-type trajectory is included for
659 comparison. Inset: illustration of halving length during folding. (I) Dynamics of angular movement
660 for representative Δ*cheY* (blue) and Δ*cheZ* (red) sister-cell pairs (2-second resolution). Inset:
661 representative wild-type example. (J) Trajectory of sister-cell angles from representative Δ*cheY*
662 example. (K) Trajectory of sister-cell angles from representative Δ*cheZ* example.
663

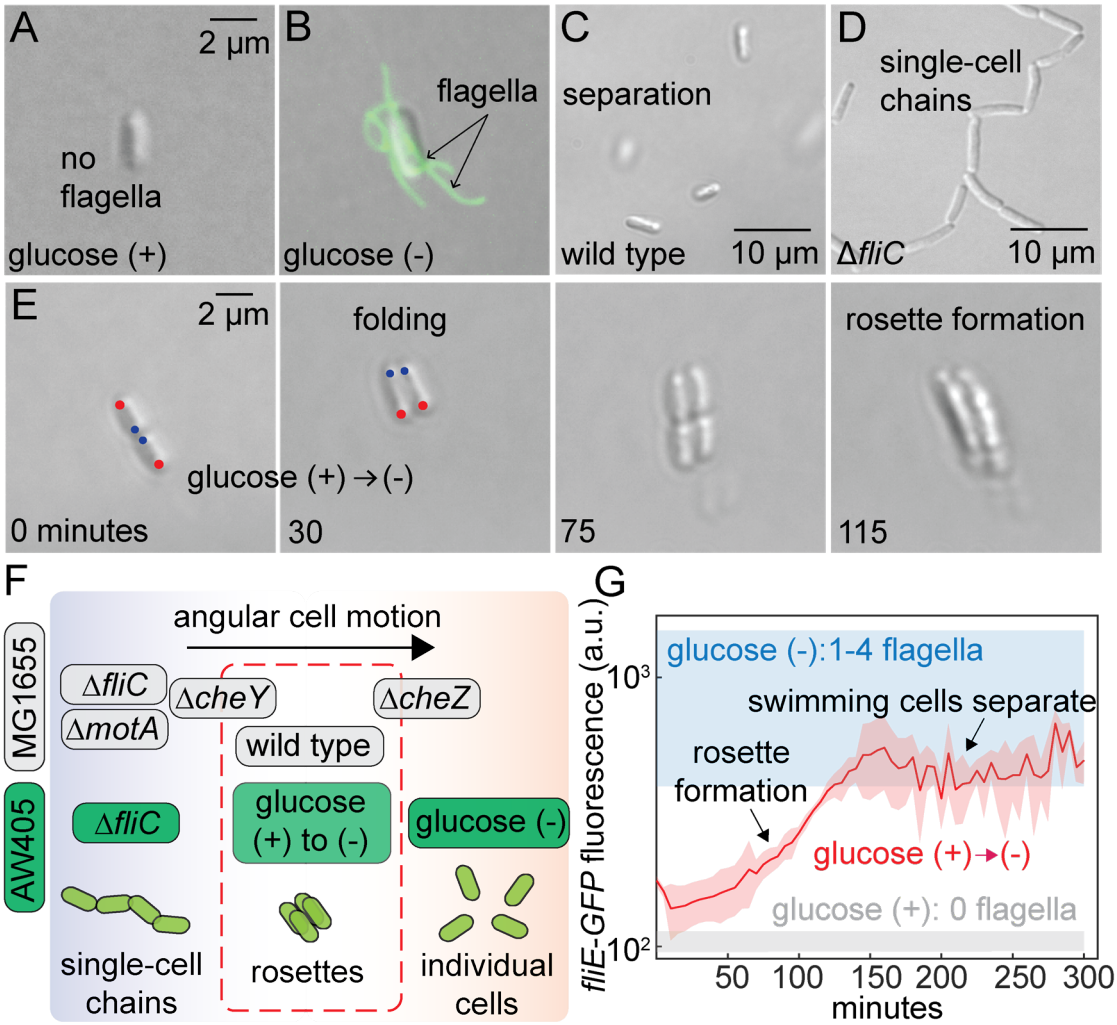

Figure 3. Rosette formation requires *de novo* flagella biosynthesis. (A) Representative micrographs of AW405 cells grown (A) with glucose and (B) without glucose and stained with Alexa Fluor 488 (green). Scale is indicated on micrographs. Micrographs from representative movies of (C) AW405 and (D) AW405 Δ*fliC* cells grown without glucose. (E) Micrographs from a representative movie of AW405 transitioned from glucose (+) to glucose (-) media. New (blue) and old (red) poles are indicated. (F) Diagram of the observed angular cell motion of strains and conditions used throughout this study and correspondence to community structure. Δ*cheY* and Δ*cheZ* cells produce heterogeneous outcomes and hence overlap depicted multicellular regions.

674 (G) Cellular fluorescence (arbitrary units) from *fliE-GFP* promoter reporter during chain
675 morphogenesis (red) in AW405 on transition from glucose (+) to (-) (5-minute resolution; mean ±
676 standard deviation, n=3). Grey zone indicates *fliE-GFP* fluorescence in non-flagellated cells in
677 glucose (+) media (see Fig. S37). Blue zone indicates *fliE-GFP* cellular fluorescence in flagellated
678 cells (1-4 flagella per cell) in glucose (-) media (see Fig. S37). The approximate times of rosette
679 formation and dissociation of single swimming cells are indicated by arrows.
680

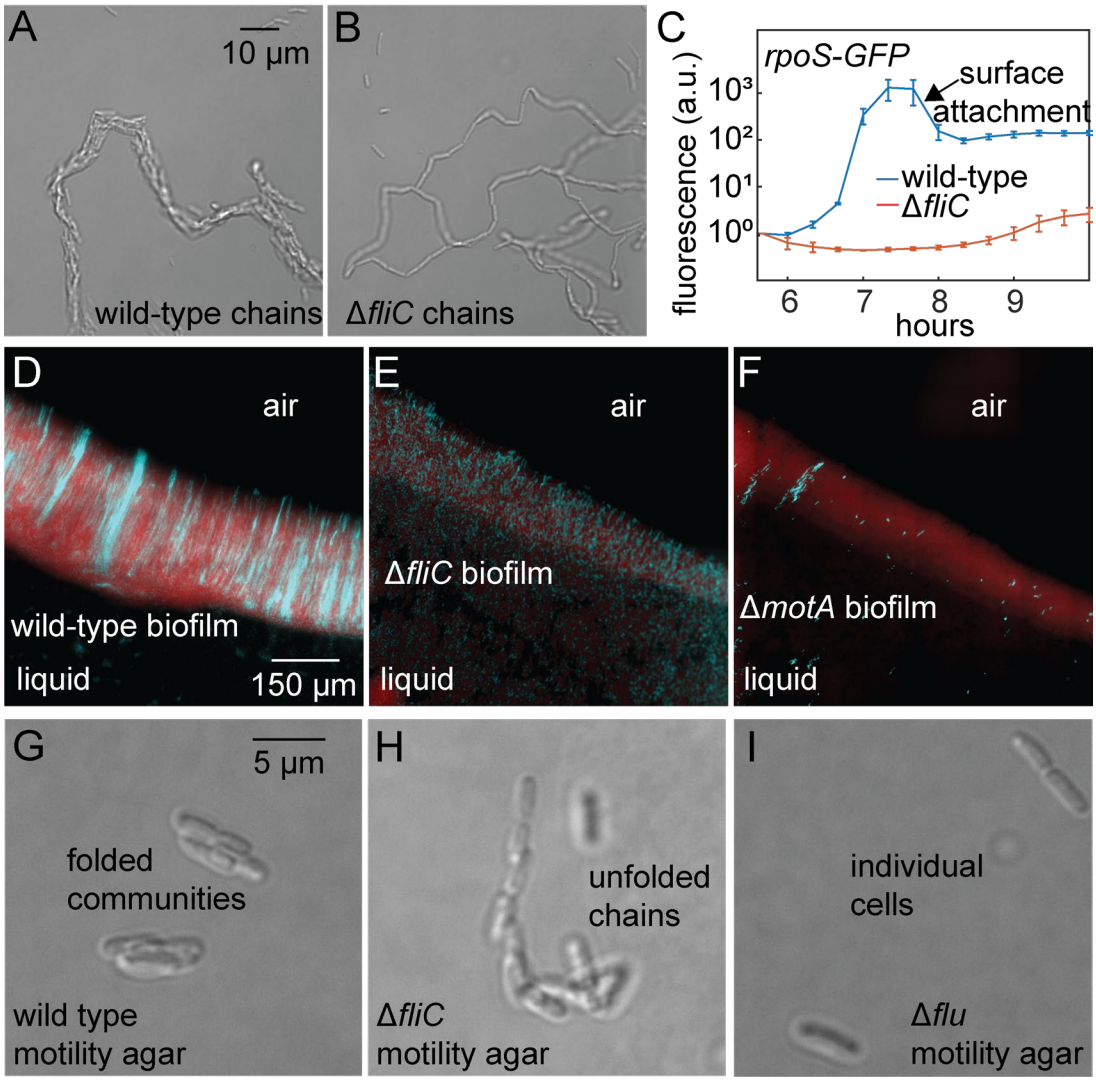

Figure 4. Developmental consequences and generality of rosette formation**.** Micrographs at 5 hours from representative movies of (A) wild-type and (B) Δ*fliC* community formation (scale is indicated). (C) Cellular fluorescence (arbitrary units) from *rpoS-GFP* promoter reporter during chain morphogenesis in wild type (blue) and Δ*fliC* (red) (20-minute resolution; mean ± standard deviation, n=3). The approximate time of chain attachment to surfaces is indicated. Micrographs of hydrostatic biofilms formed by (D) wild-type, (E) Δ*fliC*, and (F) Δ*motA* cells. Cells contained either mScarlet (red) or GFP (cyan) at a 10:1 ratio (scale, as well as air and liquid sides of biofilms,

690 are indicated). Example micrographs of (G) wild-type, (H) Δ*fliC*, and (I) Δ*flu* cells after ~2 hours

691 on motility agar (2-layer 0.25% agar; scale is indicated; see also Fig. S40).

692

693

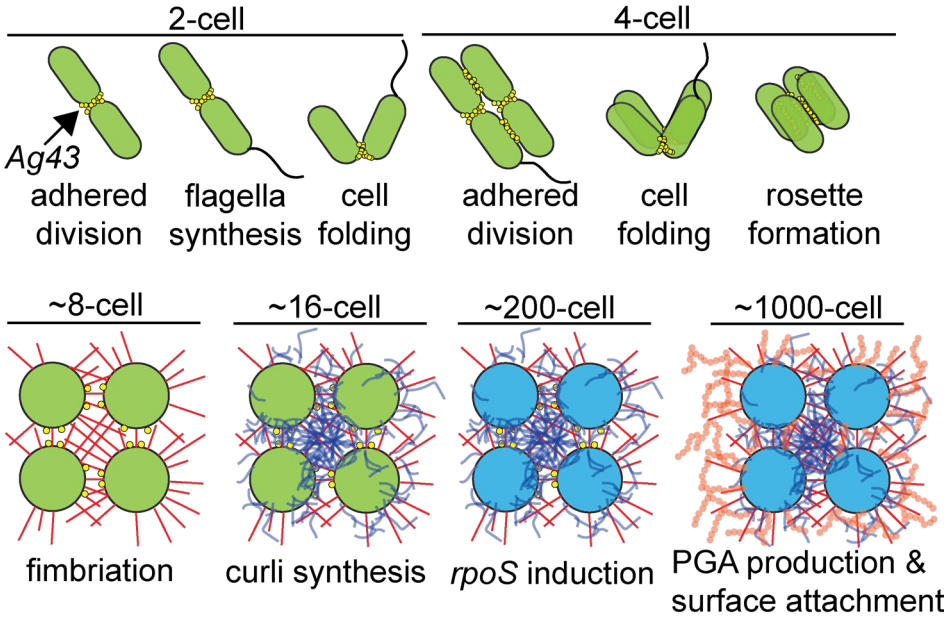

694

695 **Figure 5.** Stages of *E. coli* multicellular morphogenesis in hydrostatic environments. The data
696 presented here and in our previous study (6), together with past characterization of ECM-
697 comprising adhesins, support the following working model. 2-cell: self-recognizing *Ag43* enables
698 adhesion of sister cells after the first division event. Cells induce *de novo* flagella biosynthesis,
699 and the propulsion of the growing flagella tail causes sister cells to perform cell folding by an
700 angular random walk to align side by side. 4-cell: sister cells adhere after the second division
701 event and again perform cell folding to align in parallel and produce rosettes with quatrefoil
702 configuration. Rosettes transition into chains, whose square cross-sectional arrangement is
703 approximately maintained. ~8-cell stage: radial-projecting extracellular polymer type-1 fimbriae
704 (indicated in red) controls chain stability. ~16-cell stage: extracellularly polymerizing curli
705 (indicated in blue) maintains cellular positioning. ~200-cell stage: transcriptional master regulator
706 σ^{38} (encoded by *rpoS*) is induced (indicated by cells turning blue). ~1000-cell stage: extracellular
707 polysaccharide poly-b-1,6-N-acetyl-D-glucosamine (PGA, indicated in orange) is produced and

708 attaches multicellular communities to surfaces. The representations of adhesins are not to scale

709 and have yet to be confirmed by electron microscopy.